



# Dense Cores, Filaments, and Outflows in the S255IR Region of High-mass Star Formation

Igor I. Zinchenko<sup>1</sup> , Sheng-Yuan Liu<sup>2</sup> , Yu-Nung Su<sup>2</sup>, Kuo-Song Wang<sup>2</sup> , and Yuan Wang<sup>3</sup>

<sup>1</sup> Institute of Applied Physics of the Russian Academy of Sciences 46 Ul'yanov str., 603950 Nizhny Novgorod, Russia; [zin@appl.sci-nnov.ru](mailto:zin@appl.sci-nnov.ru)

<sup>2</sup> Institute of Astronomy and Astrophysics, Academia Sinica P.O. Box 23-141, Taipei 10617, Taiwan, R.O.C.

<sup>3</sup> Max-Planck-Institut für Astronomie Königstuhl 17, D-69117 Heidelberg, Germany

Received 2019 August 10; revised 2019 November 25; accepted 2019 November 25; published 2020 January 23

## Abstract

We investigate at a high angular resolution the spatial and kinematic structure of the S255IR high-mass star-forming region, which demonstrated recently the first disk-mediated accretion burst in the massive young stellar object. The observations were performed with the Atacama Large Millimeter/submillimeter Array (ALMA) in Band 7 at an angular resolution of  $\sim 0''.1$ , which corresponds to  $\sim 180$  au. The 0.9 mm continuum,  $C^{34}S(7-6)$  and CCH  $N = 4 - 3$  data show a presence of very narrow ( $\sim 1000$  au), very dense ( $n \sim 10^7$  cm $^{-3}$ ), and warm filamentary structures in this area. At least some of them represent apparently dense walls around the high velocity molecular outflow with a wide opening angle from the S255IR-SMA1 core, which is associated with the NIRS3 YSO. This wide-angle outflow surrounds a narrow jet. At the ends of the molecular outflow there are shocks, traced in the SiO(8-7) emission. The SiO abundance there is enhanced by at least 3 orders of magnitude. The CO(3-2) and SiO(8-7) data show a collimated and extended high velocity outflow from another dense core in this area, SMA2. The outflow is bent and consists of a chain of knots, which may indicate periodic ejections possibly arising from a binary system consisting of low- or intermediate-mass protostars. The  $C^{34}S$  emission shows evidence of rotation of the parent core. Finally, we detected two new low-mass compact cores in this area (designated as SMM1 and SMM2), which may represent prestellar objects.

*Unified Astronomy Thesaurus concepts:* [Star formation \(1569\)](#); [Interstellar molecules \(849\)](#); [Stellar winds \(1636\)](#); [Stellar jets \(1607\)](#); [Massive stars \(732\)](#)

## 1. Introduction

The process of massive star formation attracts an enhanced attention nowadays. This is caused by serious problems in theoretical understanding of this phenomenon and difficulties in its observational studies, which are related to the rarity and large distances of high-mass star-forming (HMSF) regions. There are a number of recent works on this subject, both observational and theoretical. Most of the results are summarized in several reviews (e.g., McKee & Ostriker 2007; Zinnecker & Yorke 2007; Krumholz et al. 2009; Krumholz 2012; Tan et al. 2014; Motte et al. 2018). A crucial question is whether this process can be considered as a scaled-up version of the low-mass star formation or not. In this respect observations of the phenomena related to the disk accretion scenario in HMSF regions are very important.

Recently this scenario got strong support from observations of the first disk-mediated accretion burst in the massive ( $\sim 20 M_{\odot}$ ) young stellar object S255 NIRS3 (Caratti O Garatti et al. 2017), accompanied by the 6.7 GHz methanol maser flare (Moscadelli et al. 2017; Szymczak et al. 2018). The bolometric luminosity increased by a factor of  $\sim 5.5$  (Caratti O Garatti et al. 2017). A detailed IR light curve was obtained by Uchiyama et al. (2019). The S255IR clump has been a target for many studies over recent years. The distance to the source derived from the annual parallax measurements of water masers is  $1.78^{+0.12}_{-0.11}$  kpc (Burns et al. 2016). Observations with the SMA revealed three major cores within this clump (Wang et al. 2011; Zinchenko et al. 2012). The NIRS3 source is associated with one of them, S255IR-SMA1, which represents a disk around the massive young stellar object (Zinchenko et al. 2015). It is associated with an ionized jet (Howard et al. 1997; Cesaroni et al. 2018). Our

Atacama Large Millimeter/submillimeter Array (ALMA) data show a submillimeter burst in this object, which lasted about 2 yr (Liu et al. 2018). An even more impressive burst (with an increase by a factor of  $\sim 70$  in luminosity but with a lower initial level) was detected in another massive object, NGC 6334I-MM1 (Hunter et al. 2017). These events demonstrate the importance of the episodic disk accretion in the process of high-mass star formation. They are consistent with theoretical models, which predict disk fragmentation and episodic accretion of the fragments onto a massive protostar (Meyer et al. 2017, 2019).

Previous single-dish and interferometric studies have shown an extended outflow from S255IR, which was attributed to the SMA1 as a driving source (Wang et al. 2011; Zinchenko et al. 2015). However, our ALMA data reveal almost parallel bipolar outflows from both SMA1 and SMA2 cores (Zinchenko et al. 2018a). The outflow from SMA1 has a wide opening angle. At the same time, as mentioned above, there is a narrow ionized jet from SMA1. This suggests a two-wind outflow, which is actually expected in theoretical models (e.g., Arce et al. 2007; McKee & Ostriker 2007). However, observations of such outflows in HMSF regions are very limited (Anglada et al. 2018).

An interesting feature found in our ALMA observations of S255IR is an unusual very narrow and apparently very dense filament (Zinchenko et al. 2018a, 2018b). Interstellar filaments are now the subject of numerous investigations, since they are considered to be primary sites of star formation (e.g., André et al. 2014; Li et al. 2016).

This paper is devoted to the surroundings of this remarkable object S255IR, which are apparently strongly influenced by its activity. We present additional data on this region and discuss

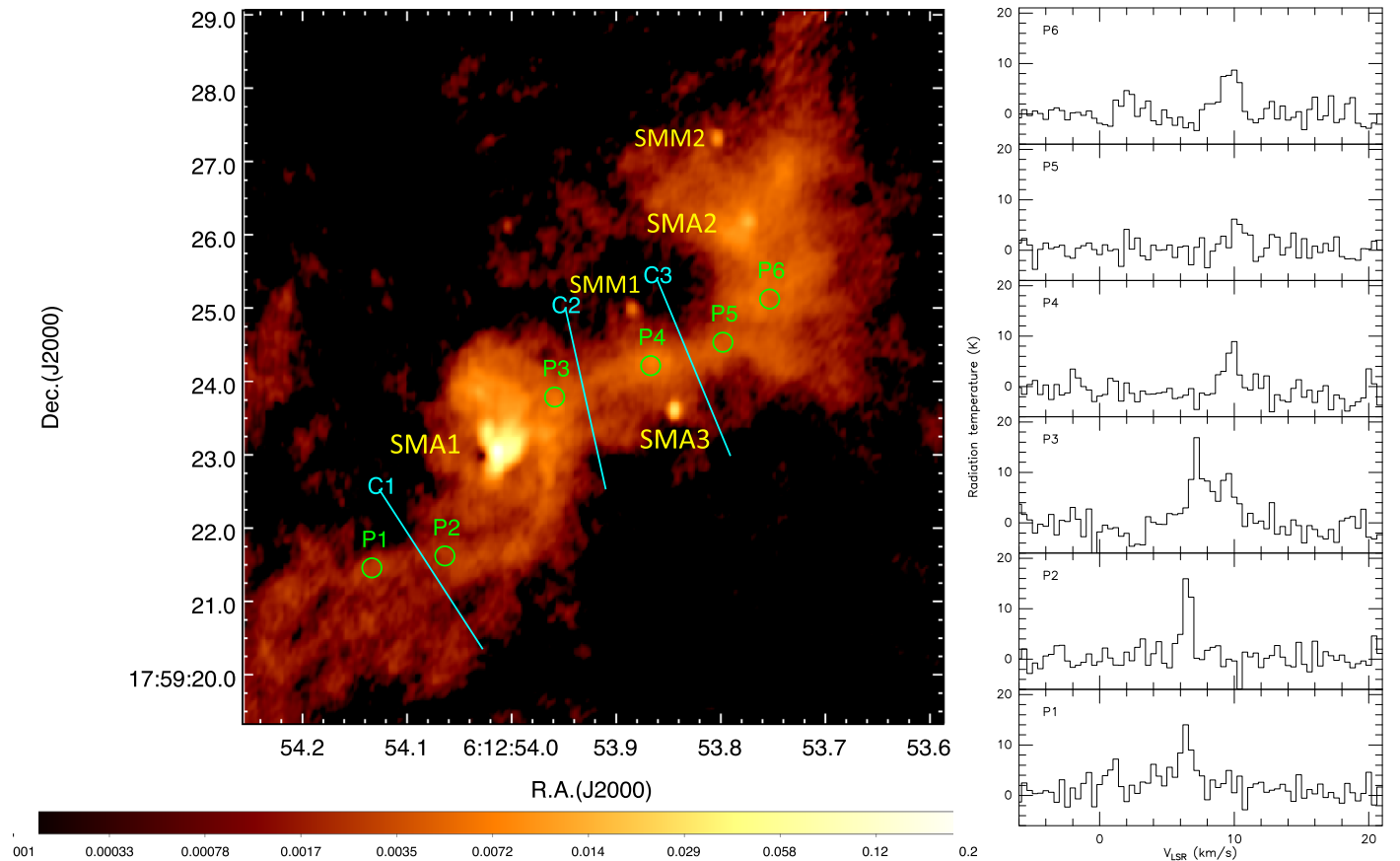


**Figure 1.** Left panel: the image of the S255IR region in continuum at 0.9 mm (logarithmic scale). The brightness scale in  $\text{Jy beam}^{-1}$  is indicated by the color bar. Several positions (P1...P6) are indicated by the green circles and three cuts (C1, C2, C3) by the cyan lines. Right panel: the  $\text{C}^{34}\text{S } J = 7 - 6$  spectra at the selected positions indicated in the left panel.

its morphology, kinematics, and physical properties with an emphasis on the new and unusual features mentioned above.

## 2. Observations

The observations were performed with ALMA in Band 7 during several observing sessions in 2016–2017 under the project 2015.1.00500.S. Details of the observations in 2016 are given in Zinchenko et al. (2017). Briefly, four spectral windows were observed, centered at around 335.4 GHz, 337.3 GHz, 349.0 GHz, and 346.6 GHz, with bandwidths of 1875.0 MHz, 234.4 MHz, 937.5 MHz, and 1875.0 MHz. Details of the observations in 2017 are given in Liu et al. (2018). The same spectral windows were observed. The projected array baselines for all sessions range between 15 m and 3.0 km.

Here we discuss the continuum emission and the  $\text{CO } J = 3 - 2$  line at 345.8 GHz,  $\text{C}^{34}\text{S } J = 7 - 6$  line at 337.4 GHz,  $\text{SiO } J = 8 - 7$  line at 347.3 GHz, and  $\text{CCH } N = 4 - 3$  lines at 349.4 GHz. The channel width was 244 kHz for  $\text{C}^{34}\text{S}$  and  $\text{CCH}$  (0.22 and 0.21  $\text{km s}^{-1}$ , respectively), and 977 kHz for  $\text{CO}$  and  $\text{SiO}$  (0.85 and 0.84  $\text{km s}^{-1}$ , respectively). The spectral resolution was twice these values with Hanning-smoothing applied. The resulting images achieve an angular resolution of  $0''.11 \times 0''.14$  (PA =  $-6^\circ.9$ ) for  $\text{C}^{34}\text{S}$ ,  $0''.11 \times 0''.14$  (PA =  $-13^\circ.0$ ) for  $\text{CCH}$ ,  $0''.10 \times 0''.15$  (PA =  $-5^\circ.3$ ) for  $\text{CO}$ ,  $0''.11 \times 0''.16$  (PA =  $4^\circ.4$ ) for  $\text{SiO}$ , and  $0''.11 \times 0''.15$  (PA =  $-3^\circ.2$ ) for continuum with Briggs weighting with a robust parameter of 0.5.

## 3. Results

We present the measurement results in the flux density units and/or in the Rayleigh–Jeans temperature scale, which is just a linear measure of intensity. It is frequently defined as the radiation temperature ( $T_R$ ) and is related to the source parameters by the simple expression, which follows from the equation of radiative transfer (e.g., Mangum & Shirley 2015):

$$T_R = f [J_\nu(T) - J_\nu(T_{\text{bg}})] [1 - \exp(-\tau_\nu)], \quad (1)$$

where

$$J_\nu(T) \equiv \frac{\frac{h\nu}{k}}{\exp\left(\frac{h\nu}{kT}\right) - 1}, \quad (2)$$

$h$  is the Planck constant,  $k$  is the Boltzmann constant,  $f$  is the so-called beam filling factor,  $\tau_\nu$  is the source optical depth. The temperature  $T$  here can be the excitation temperature of the considered molecular transition or the dust temperature. It is assumed to be constant along the line of sight.  $T_{\text{bg}}$  is the background temperature, which usually refers to the temperature of the cosmic microwave background radiation.

The ALMA image of the S255IR region in continuum at 0.9 mm is shown in Figure 1. A filamentary structure can be easily seen. Several compact sources are visible, too. Among them there are three earlier identified objects, labeled SMA1, SMA2, and SMA3 (Wang et al. 2011; Zinchenko et al. 2012). The SMA1 and SMA2 clumps seem to be located within this

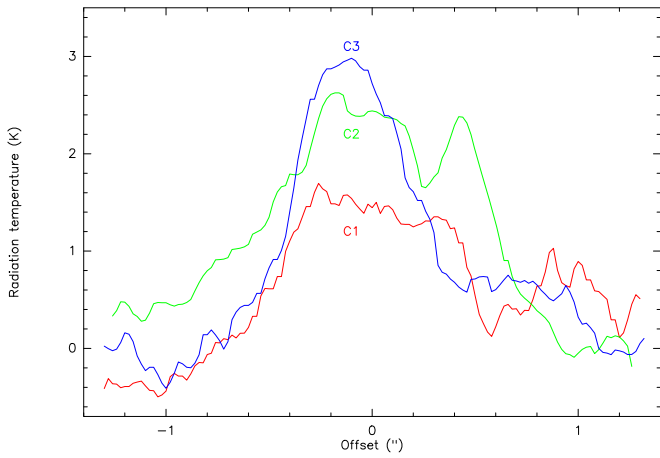


**Figure 2.** Continuum intensity profiles for three cuts across the filamentary structure (C1, C2, and C3), indicated in Figure 1.

**Table 1**

Names, Positions, Flux Densities, Deconvolved Angular Sizes, and Position Angles of the Submillimeter Wave Continuum Sources Measured at 0.9 mm

Name	$\alpha(2000)$ (h m s)	$\delta(2000)$ ( $^{\circ}$ ' ")	$S_{0.9}$ (mJy)	$\theta_{\max}$ (")	$\theta_{\min}$ (")	P.A. ( $^{\circ}$ )
SMA2	06:12:53.775	17:59:26.17	60	0.37	0.25	157
SMA3	06:12:53.843	17:59:23.62	48	0.11	0.09	8
SMM1	06:12:53.884	17:59:24.99	15	0.20	0.14	17
SMM2	06:12:53.805	17:59:27.30	10	0.15	0.12	3

structure, while the SMA3 clump looks isolated. In addition there are two more point-like sources, which we label as SMM1 and SMM2. The estimates of the fluxes and sizes of the continuum sources obtained from 2D Gaussian fit are given in Table 1. These fluxes and sizes, especially for the SMA2, are somewhat uncertain because the sources are observed on a significant background, which has a complicated morphology. We do not include in the table the SMA1 clump since its flux is variable (Liu et al. 2018) and the brightness distribution is apparently non-Gaussian. In the presented image its flux integrated in the circle of  $0''.5$  in radius centered at R.A.(J2000) =  $06^{\text{h}}12^{\text{m}}54^{\text{s}}.008$ , decl.(J2000) =  $17^{\circ}59'23''.12$  is approximately 1.04 Jy. This circle covers the brightest part of the SMA1 emission, although its size is of course still rather arbitrary. The continuum brightness along the filamentary structure, away from the major clumps, is  $\sim 2\text{--}5$  mJy beam $^{-1}$ , which corresponds to  $T_R \sim 1.5\text{--}3$  K.

The total flux density in continuum is approximately 6.6 Jy. The summary flux density of the compact cores is  $\approx 1.2$  Jy. The physical conditions in the vicinity of these cores should be different from those in the bulk of the filament. Therefore, for the estimation of the filament parameters we subtract the contribution of these clumps and arrive at an estimate for the filament flux density of 5.4 Jy.

In Figure 2 we show the intensity profiles along the cuts indicated in Figure 1. It is easy to see that the filament width at the half intensity level is  $\sim 0''.6\text{--}1''$ , which corresponds to  $\sim 1000\text{--}1800$  au. The length of the filamentary structure along the emission ridge is about  $15''$ , which corresponds to 27000 au or 0.13 pc.

In the molecular line data we see the  $\text{C}^{34}\text{S}$   $J = 7 - 6$  emission along the filament. The single pixel  $\text{C}^{34}\text{S}$  spectra at

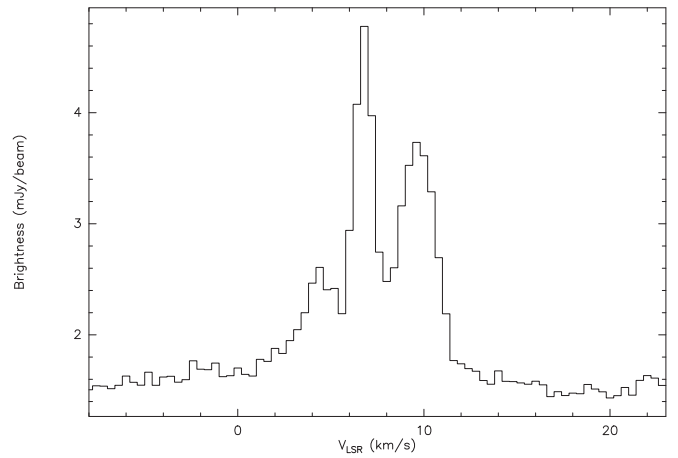


**Figure 3.** Average  $\text{C}^{34}\text{S}(7-6)$  spectrum in the S255IR area (indicated in Figure 4).

the selected positions indicated in Figure 1 (P1...P6) are shown in the same figure.

One can see that the  $\text{C}^{34}\text{S}$  velocities in the southern and in the northern parts of the filamentary structure are different. In the south the peak velocity is about  $6.5$  km s $^{-1}$ , while in the north it is about  $10$  km s $^{-1}$ . Near the SMA1 clump we see both components. The line widths of the individual components obtained from Gaussian fits taking into account instrumental broadening are from  $0.6 \pm 0.1$  km s $^{-1}$  at the P2 position to  $1.5 \pm 0.2$  km s $^{-1}$  at the P6 position.

A more detailed inspection of the data shows that the  $\text{C}^{34}\text{S}(7-6)$  emission is observed in a rather large area around the SMA1–SMA3 clumps. In the average  $\text{C}^{34}\text{S}(7-6)$  spectrum three main velocity components can be distinguished (Figure 3). In addition to the two components mentioned above, there is an emission peak at  $\sim 4$  km s $^{-1}$ . A general picture of the  $\text{C}^{34}\text{S}$  emission in this area is presented in Figure 4. The three main velocity components, at  $4$  km s $^{-1}$ ,  $6.5$  km s $^{-1}$ , and  $10$  km s $^{-1}$ , are shown by the blue, green, and red colors, respectively. It is worth mentioning that the systemic velocity of the SMA1 clump is about  $5$  km s $^{-1}$  (Zinchenko et al. 2015).

Figure 4 shows that distributions of the dust continuum and  $\text{C}^{34}\text{S}$  emission are significantly different. Some regions of a rather strong  $\text{C}^{34}\text{S}$  emission have no noticeable counterpart in continuum. A more detailed picture of the spatial and kinematic distribution of the  $\text{C}^{34}\text{S}$  emission is presented in the channel maps (Figure 5).

A further inspection of the ALMA data shows a rather strong emission in the CCH lines in this area. The four strongest components of the  $N = 4 - 3$  transition are observed:  $J = 9/2 - 7/2$ ,  $F = 5 - 4$ ;  $J = 9/2 - 7/2$ ,  $F = 4 - 3$ ;  $J = 7/2 - 5/2$ ,  $F = 4 - 3$ ; and  $J = 7/2 - 5/2$ ,  $F = 3 - 2$  with the excitation energies of the upper levels of about 41.9 K. In some parts the weaker  $J = 7/2 - 5/2$ ,  $F = 3 - 3$  component is also seen. The emission is rather well correlated spatially with the  $10$  km s $^{-1}$   $\text{C}^{34}\text{S}$  component (Figure 6). The radiation temperature in the CCH lines reaches approximately 37 K at the emission peak.

The detection of the weaker CCH line allows an estimation of the optical depth in the CCH lines under the assumption of the same excitation temperature for all transitions. The ratio of the intensities of the strongest  $J = 9/2 - 7/2$ ,  $F = 5 - 4$  transition and the weak  $J = 7/2 - 5/2$ ,  $F = 3 - 3$  transition is  $11 \pm 1$ .

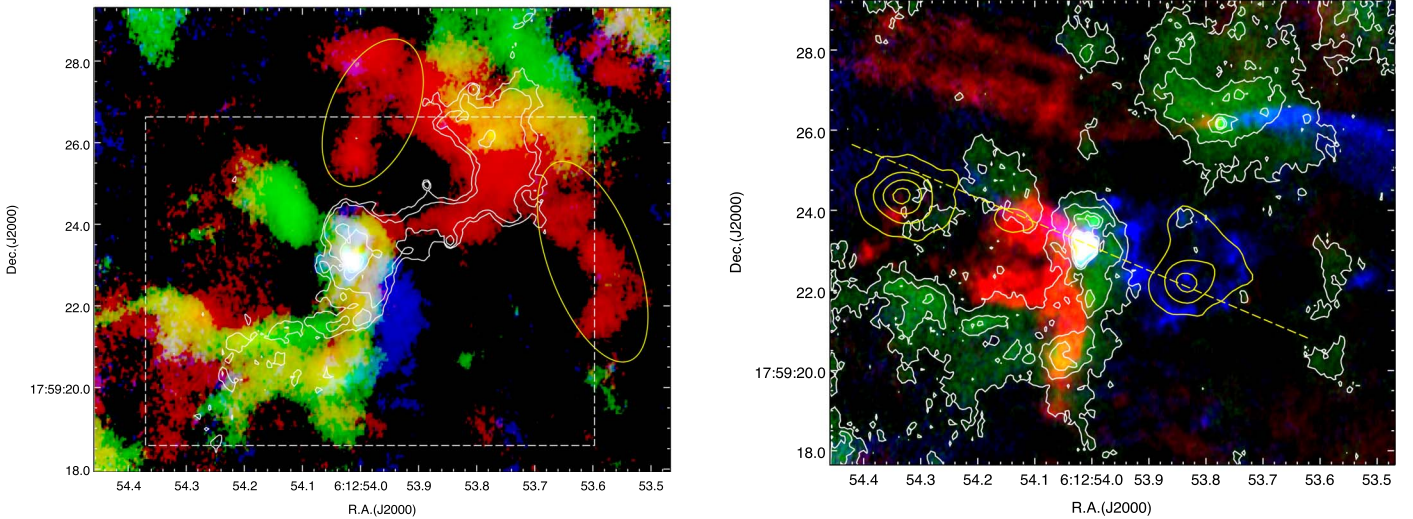


**Figure 4.** Left panel: a three-color map of the  $C^{34}S J = 7 - 6$  emission in the S255IR area. The emission in the velocity intervals  $9-11 \text{ km s}^{-1}$ ,  $5.5-7.5 \text{ km s}^{-1}$  and  $3-5 \text{ km s}^{-1}$  is shown in red, green, and blue colors, respectively. The white contours show the continuum emission at  $0.9 \text{ mm}$  as in Figure 1. The contour levels are at 2, 3, 9, 42.5, and  $230 \text{ mJy beam}^{-1}$ . The dashed rectangle shows the area used to compute the average  $C^{34}S$  spectrum in Figure 3. The ellipses indicate the arc-like structures discussed in the text. Right panel: the red and blue colors show the high velocity redshifted (integrated in the velocity range from  $20$  to  $90 \text{ km s}^{-1}$ ) and blueshifted (integrated in the velocity range from  $-67$  to  $-16 \text{ km s}^{-1}$ )  $CO(3-2)$  emission, respectively. The  $C^{34}S$  emission integrated in the velocity range  $1-13 \text{ km s}^{-1}$  is shown in green and by the white contours. The contour levels are from  $20$  to  $200 \text{ mJy beam}^{-1} \text{ km s}^{-1}$  in step of  $45 \text{ mJy beam}^{-1} \text{ km s}^{-1}$ . The yellow contours show the Fe II emission (Wang et al. 2011). The dashed line indicates the jet axis as found by Howard et al. (1997) from near-IR  $H_2$  and  $Br\gamma$  images.

At the same time the ratio of the line strengths of these lines is  $\approx 29.2$  (CDMS—Müller et al. 2005; Endres et al. 2016). This gives us immediately estimates of the optical depths in the weaker transition of  $\approx 0.08$  and for the strongest transition of  $\approx 2.4$ . From Equation (1) assuming the beam filling factor equals unity we obtain the excitation temperature  $T_{\text{ex}} \approx 50 \text{ K}$ . This gives us a lower limit for the kinetic temperature.

However, the assumption of the equal excitation temperatures for different transitions needs a justification. We modeled the CCH excitation with RADEX (van der Tak et al. 2007). This modeling shows that the observations are best reproduced at densities  $n \gtrsim 10^7 \text{ cm}^{-3}$ ,  $T_{\text{kin}} = 55 \text{ K}$  and CCH column density  $N(\text{CCH}) \approx 5 \times 10^{15} \text{ cm}^{-2}$ . A reasonable fit can be obtained at  $n = 3 \times 10^6 \text{ cm}^{-3}$ ,  $T_{\text{kin}} = 60 \text{ K}$ . At lower densities the excitation of different components becomes significantly different and the intensity ratios for the stronger components are inconsistent with the observations.

The CCH radiation temperature peaks in the area of the maximum CCH integrated intensity near the SMA2 core. Although in the other parts the radiation temperature is lower and the optical depth is also lower, as indicated by the line ratios. The estimates show that in some areas the excitation temperature can be even higher than at the emission peak (but the uncertainties of these estimates are rather large). Actually this emission peak is not associated with any heating source, so there is no apparent physical reason for an enhanced temperature at this position. Most probably the peak of the radiation temperature is explained by a higher CCH optical depth here.

In the right panel of Figure 4 the high velocity  $CO(3-2)$  emission in the blue- and redshifted wings is shown in blue and red colors, respectively. A more detailed picture of the CO kinematics is given in Figure 7, where we present channel maps of the blueshifted and redshifted high velocity  $CO(3-2)$  emission.

In some parts of this area we also see a rather strong  $SiO(8-7)$  emission (Figure 8). In particular it is observed toward the region

outlined by the dashed box in Figure 8. The close-up view of this region with an addition of the Fe II emission is presented in Figure 9. The  $SiO(8-7)$  and  $C^{34}S(7-6)$  spectra averaged over the area marked by the yellow circle in this figure are shown in Figure 10. In Figure 11 we present the position–velocity diagrams for these lines along the path indicated in Figure 9.

## 4. Discussion

### 4.1. General Structure and Kinematics of S255IR

Our  $C^{34}S$  and CCH data reveal a rather complicated morphology and kinematics of the region. At first glance they indicate the presence of several intersecting filamentary structures. However, a comparison with the high velocity  $CO(3-2)$  emission (Figure 4) and with the  $SiO$  emission (Figures 8, 9) reveals another picture. One can see that a strong  $C^{34}S$  emission surrounds a part of the redshifted lobe of the high velocity outflow from the SMA1 core. Apparently this emission originates in the dense walls of the outflow cavity. This view is supported by observations of the  $CO$  emission at the interface of the  $CO$  and  $C^{34}S$  emission regions (Figures 8, 9). It is well known that an enhanced  $SiO$  emission usually traces shocked regions. Actually the morphology of the redshifted outflow lobe is rather complicated. There is the “main” outflow around the jet and an additional stream in the south direction, which is also associated with the  $SiO$  emission. This can indicate that the “wall” is not perfect, there may be “holes” in the wall.

Since the critical density for the  $C^{34}S(7-6)$  transition is  $\sim 10^7 \text{ cm}^{-3}$  (e.g., Codella et al. 2014), the gas density in these walls should be at least close to this value. In principle a noticeable emission can arise at much lower densities (Shirley 2015) but it requires a high optical depth in the lines and correspondingly high column density. The numerical estimates will be given below.

The similarity of the morphology of the CCH and  $C^{34}S$  emission hints at their common origin. Observations of dense outflow walls in the CS and CCH lines have been reported

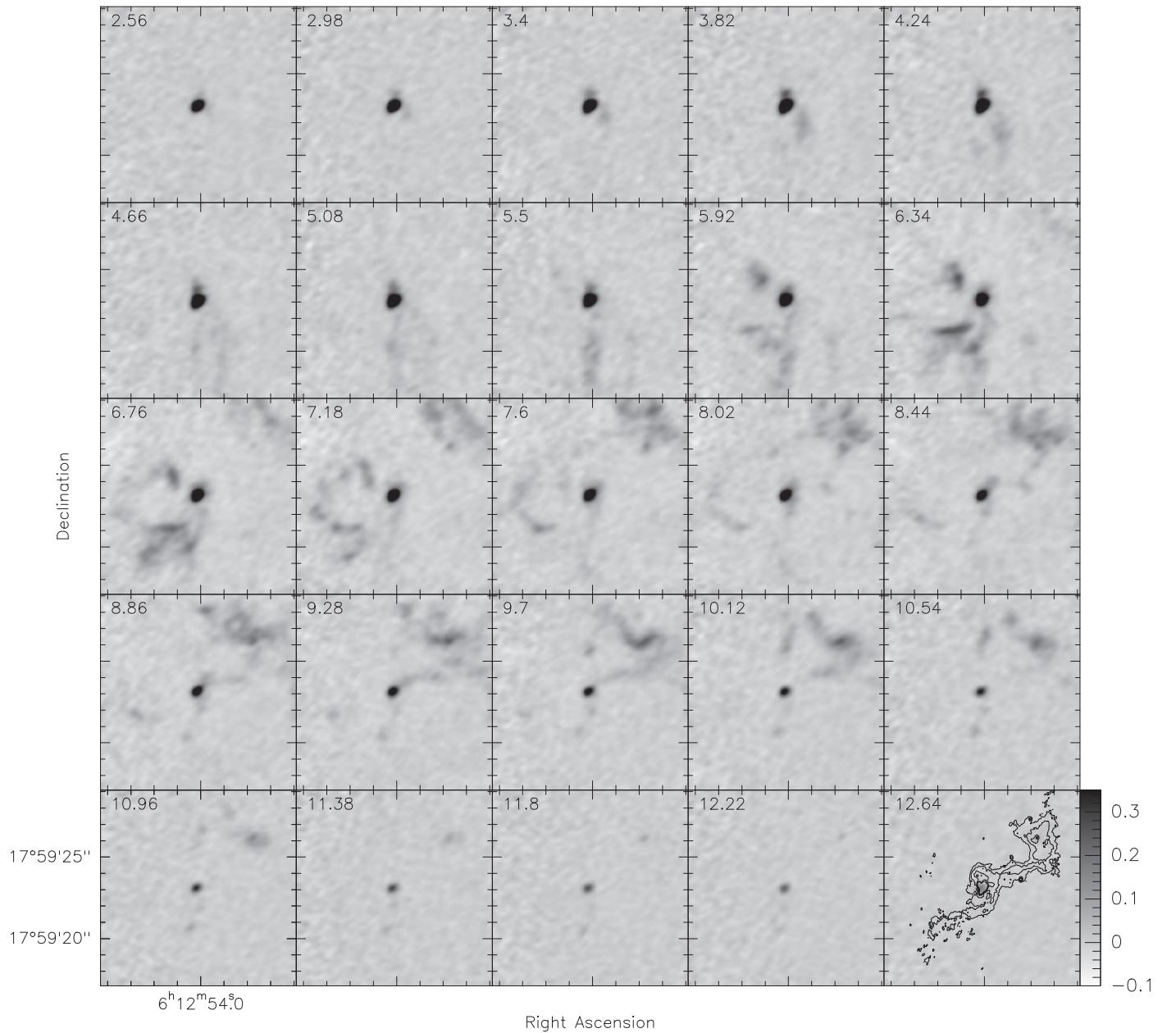


**Figure 5.** Channel maps of the  $C^{34}S(7-6)$  emission in the S255IR area. The center velocities are indicated in the upper left corner of each panel. The channel width is  $0.42 \text{ km s}^{-1}$ . The tick spacing at the R.A. axis is  $0.1''$ . The color bar indicates the intensity scale (in  $\text{Jy beam}^{-1}$ ). The contours in the last panel show the 0.9 mm continuum emission. The contour levels are at 2, 4, 8, 12, and  $16 \text{ mJy beam}^{-1}$ .

recently for both low-mass and HMSF regions (Bruderer et al. 2009a; Gómez-Ruiz et al. 2015; Oya et al. 2015, 2018; Leung et al. 2016; Zhang et al. 2018). The reasons for enhancement of the abundances of these molecules are discussed in these works. Briefly, the CS abundance increases sharply at  $T > 100 \text{ K}$  due to the evaporation of sulfur from dust grains. CCH can be formed in photodissociation regions created by the UV radiation from the central protostar. It can also be formed in the envelope via warm carbon-chain chemistry. Both the high brightness temperatures in the  $C^{34}S$  and CCH lines, and these chemical models indicate that the temperature in the walls can be rather high,  $\gtrsim 100 \text{ K}$ . The walls can be heated to rather high temperatures by the UV radiation from the massive protostar (e.g., Bruderer et al. 2009a, 2009b) or by the energy transfer from the high velocity gas (e.g., Hatchell et al. 1999).

Unfortunately the assumption of such high temperature cannot be confirmed by the available observational data. The radiation temperature in the  $C^{34}S(7-6)$  line reaches approximately  $40 \text{ K}$  in the area shown in Figure 9. In case of a high optical depth and the beam filling factor equal to unity this implies the excitation temperature of  $\approx 48 \text{ K}$ , which places a lower limit on the kinetic temperature.

We note, however, that the other outflow in this area, originating at the SMA2 core, shows no associated  $C^{34}S$  or CCH emission.

In this picture the nature of the filamentary structure seen in continuum is not very clear. It is located between the redshifted and blueshifted outflow lobes with wide opening angles and may be influenced by both of them. It is not excluded that it is a part of these walls. The CS and CCH relative abundances in

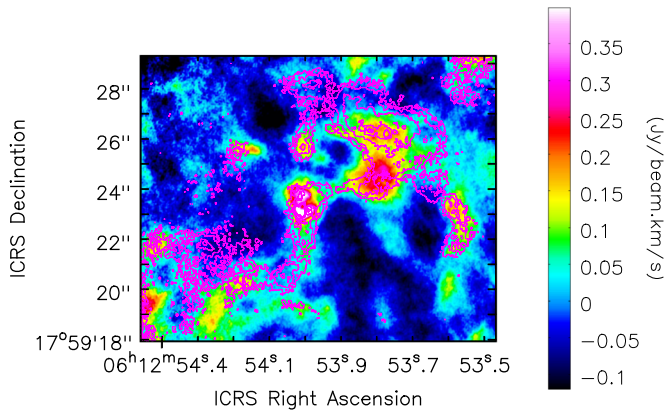


**Figure 6.** Image of the CCH  $N = 4 - 3$  integrated emission overlaid with contours of the  $C^{34}S J = 7 - 6$  emission in the  $10 \text{ km s}^{-1}$  component. The contour levels are at 10, 20, to 100 in step of  $20 \text{ mJy beam}^{-1} \text{ km s}^{-1}$ . Around the SMA1 core the CCH lines are blended with other strong lines.

this structure are probably lower than in the walls discussed above, where no noticeable continuum emission is detected. The temperature may be lower, too, but not less than the CCH excitation temperature discussed above. We assume the kinetic temperature in the continuum filament to be 50 K. Since the preliminary estimates indicate a rather high gas density  $\sim 10^8 \text{ cm}^{-3}$  (Zinchenko et al. 2018a), the dust and gas temperatures should be tightly coupled (e.g. Banerjee et al. 2006), so the dust temperature may be assumed to be equal to the gas temperature.

The continuum radiation temperature along the continuum filament is  $\sim 2-3 \text{ K}$ . This implies the optical depth of  $\sim 0.06$ . Assuming the dust opacity at this wavelength of  $1.8 \text{ cm}^2 \text{ g}^{-1}$  according to Ossenkopf & Henning (1994) we obtain the dust column density  $\sim 0.03 \text{ g cm}^{-2}$  and assuming the mean molecular weight per hydrogen molecule of 2.8 (Kauffmann et al. 2008), we further estimate the  $H_2$  column density  $\sim 7 \times 10^{23} \text{ cm}^{-2}$ . Assuming the thickness of the filament the same as its width ( $\sim 1500 \text{ au}$ ) we obtain the mean hydrogen volume density  $n \sim 3 \times 10^7 \text{ cm}^{-3}$ . Both the inferred column density and the volume density are lower than the preliminary values mentioned earlier (Zinchenko et al. 2018a) as the adopted dust temperature here is higher. However, the thickness of this structure may be larger than the observed width and therefore this value for density should be considered as an upper limit. The total mass of the filamentary structure seen in continuum is about  $35 M_{\odot}$  (under the assumption of the dust temperature equal to 50 K).

Our non-LTE modeling with RADEX (van der Tak et al. 2007) under the assumptions of  $T = 50 \text{ K}$ ,  $n = (1-3) \times 10^7 \text{ cm}^{-3}$ , and  $\Delta V = 1.5 \text{ km s}^{-1}$  for the CS  $J = 7 - 6$  transition ( $C^{34}S$  is absent in the RADEX database) gives an estimate for the  $C^{34}S$  column density  $N(CS) \sim 5 \times 10^{13} \text{ cm}^{-2}$ , which implies the  $C^{34}S$  relative abundance  $X(C^{34}S) \sim 7 \times 10^{-11}$ . The optical depth in the line is  $\sim 0.3$ . This estimate is consistent with the typical values of the  $C^{34}S$  abundance in HMSF cores (e.g., Shirley et al. 2003) although an order of magnitude lower than our estimate for S255 from single-dish observations (Zinchenko et al. 2009). The fit for  $n = 10^6 \text{ cm}^{-3}$  gives  $N(C^{34}S) \sim 2 \times 10^{14} \text{ cm}^{-2}$  and the optical depth in the line  $\sim 1.7$  (even higher in the lower transitions). This implies a huge optical depth in the lines of the main isotopologue. Taking into account the results of the CCH excitation analysis,

we prefer the density estimate of  $n = (1-3) \times 10^7 \text{ cm}^{-3}$ , which is consistent with the  $C^{34}S$ , CCH and continuum data.

However, in the regions of the strong  $C^{34}S$  emission without continuum counterpart the  $C^{34}S$  relative abundance should be much higher if the dust to gas mass ratio has the “standard” value. Under this assumption, the hydrogen column density in these regions should be at least several times lower than that in the continuum filament, in order to explain the absence of the continuum emission. This implies also a lower value of the mean volume density in these regions. As shown above, the observed  $C^{34}S(7-6)$  line can be modeled at relatively low densities  $n = (1-3) \times 10^6 \text{ cm}^{-3}$ . For example, at  $T_{\text{kin}} = 100 \text{ K}$  and  $n = 3 \times 10^6 \text{ cm}^{-3}$  the required  $C^{34}S$  column density is  $N(C^{34}S) \sim 2.2 \times 10^{14} \text{ cm}^{-2}$  with the optical depth in the line  $\sim 1.3$ . This implies the CS relative abundance of  $\sim 10^{-7}$ , which is close to the highest values obtained in the models (Bruderer et al. 2009a). These requirements can be relaxed by assuming that the “wall” structure may have a clumpy nature, with which the absence of strong continuum emission results from the relatively low mean volume density and the  $C^{34}S$  excitation is achieved in high density clumps. Figure 9 shows that the  $C^{34}S$  distribution may be rather inhomogeneous on small scales, indeed. An alternative explanation can be based on the reduced dust to gas mass ratio. The dust grains can be destructed by shocks or swept out somehow. The destruction usually leads to an enhanced SiO abundance, which we do observe in some compact regions (see below). However, there is no sign that such a process could happen in the rather extended areas of the significant  $C^{34}S$  emission outside the continuum “filament.” The swept-out dust should be seen somewhere, but we do not see this. Therefore we conclude that this alternative explanation can be rejected.

#### 4.2. Outflow from SMA1

The outflow from SMA1, as observed in CO(3-2), has a wide opening angle. At the same time the compact Fe II emission at the ends of the outflow lobes (Figure 4), which coincides with the radio continuum knots observed with the Very Large Array (VLA; Cesaroni et al. 2018) indicates the presence of strong bow shocks. There is probably a narrow jet, creating these bow shocks, and a surrounding wind with a wide opening angle. The orientation of the redshifted jet is apparently somewhat different from that found by Howard et al. (1997) (which is indicated by the dashed line in Figure 4). The radio continuum data imply the presence of the ionized gas, which is apparently concentrated in the narrow jet (Zinchenko et al. 2015; Cesaroni et al. 2018). Such a picture is consistent with the existing outflow models (e.g., Arce et al. 2007) but has been observed mainly in low-mass protostars (Anglada et al. 2018). Probably the best example of such two-wind outflow from a massive protostar is Cep A HW2, where a fast narrow jet and a slower wide-angle outflow have been identified from the water maser observations (Torrelles et al. 2011).

In our case the CO emission is relatively weak along the outflow axis and peaks near the outflow walls. A rather strong SiO emission is observed mainly at the edges of high velocity flows traced in CO, especially in the redshifted outflow lobe (Figure 8). In particular near the position outlined by the dashed box in Figure 8 it looks like a narrow lane oriented perpendicular to the CO flow (at its end). It is most likely

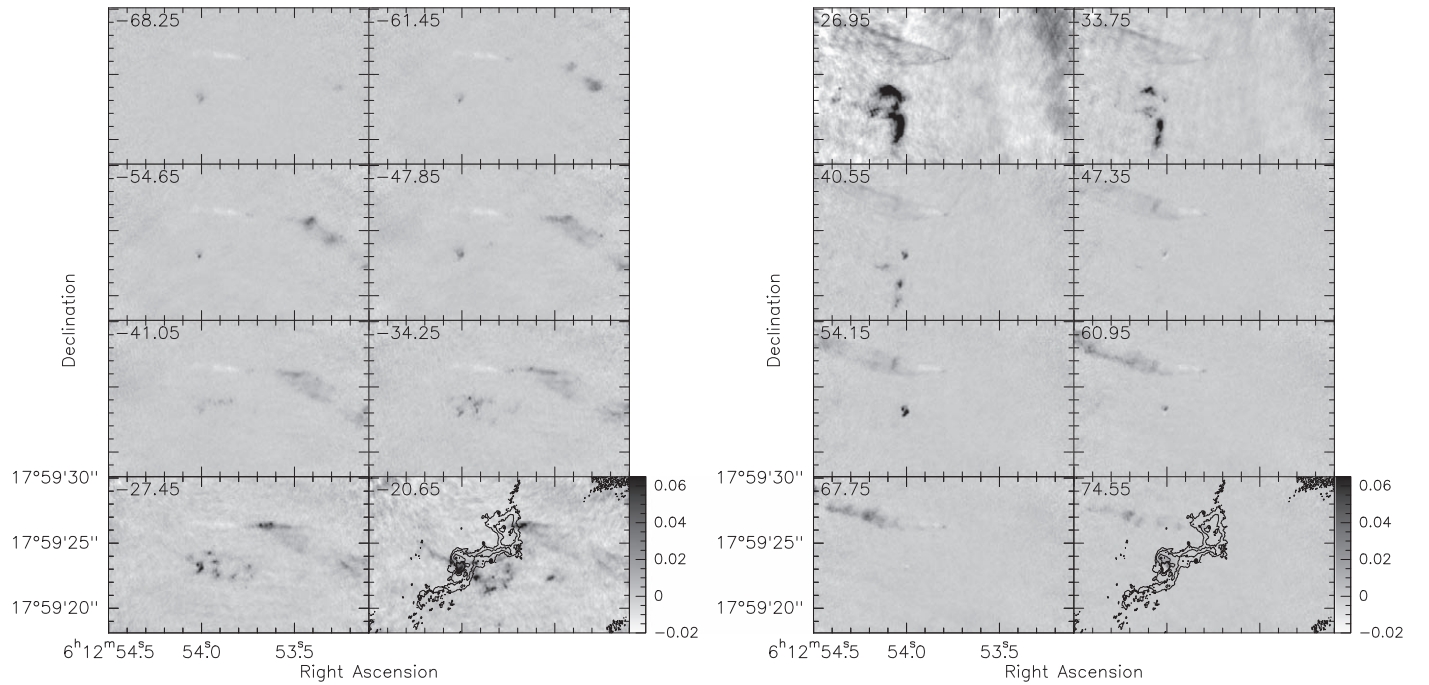


**Figure 7.** Channel maps of the high velocity CO(3–2) blueshifted (left panel) and redshifted (right panel) emission in the S251R area. The center velocities are indicated in the upper left corner of each panel. The channel width is  $6.8 \text{ km s}^{-1}$ . The contours in the last panel show the 0.9 mm continuum emission. The color bar indicates the intensity scale (in  $\text{Jy beam}^{-1}$ ).

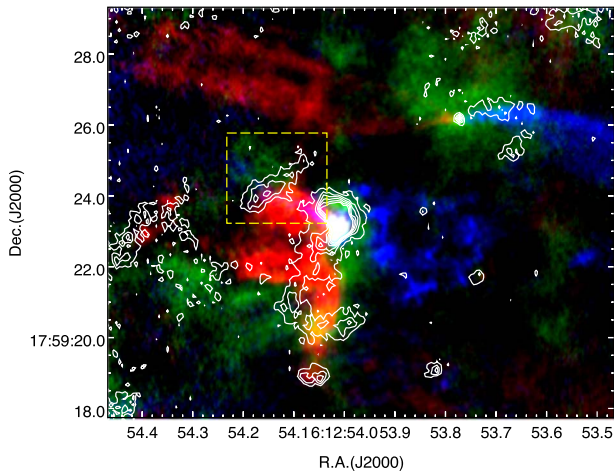


**Figure 8.** Image: the SiO(8–7) integrated emission map (white contours) overlaid on the map of the high velocity CO(3–2) emission (red and blue colors). The integrated  $\text{C}^{34}\text{S}(7-6)$  emission is shown in green. The contour levels are at 75 to 450 in step of  $75 \text{ mJy beam}^{-1} \text{ km s}^{-1}$ .

associated with a shock, as usually expected for SiO. The morphology of the SiO emission is consistent with this assumption (e.g., Masson & Chernin 1993).

Figures 8 and 11 show that the peak of the SiO emission is located at the inner side of the  $\text{C}^{34}\text{S}$  wall, although a fainter emission is also observed beyond the wall. The SiO and  $\text{C}^{34}\text{S}$  velocities are significantly different (Figures 11, 10). In principle the SiO and  $\text{C}^{34}\text{S}$  emission regions can be spatially separated on the line of sight. However, there are signs of interaction between them. While the SiO velocity increases toward the wall on the inner side, it begins to decrease on the other side. The  $\text{C}^{34}\text{S}$  velocity dispersion is somewhat larger on the inner side of the wall. A significant velocity difference between the wall and the

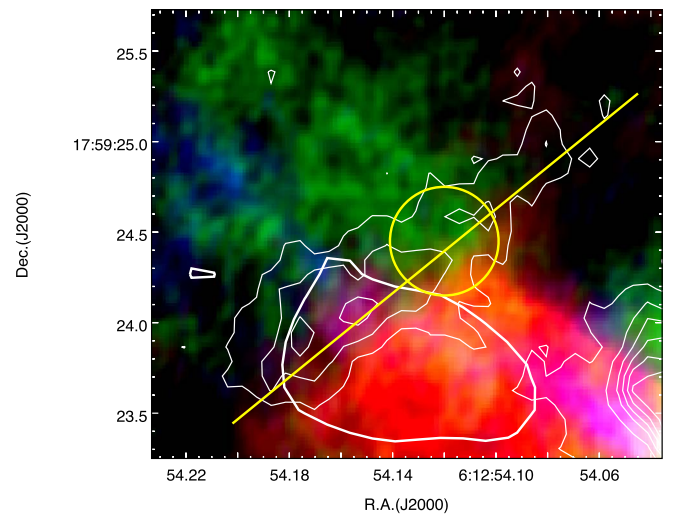


**Figure 9.** Close-up view of the region marked by the dashed box in Figure 8. The thick white contours show the Fe II emission. The yellow circle indicates the position, where the SiO(8–7) and  $\text{C}^{34}\text{S}(7-6)$  spectra are presented in Figure 10, and along the yellow line the position–velocity diagrams for these lines are shown in Figure 11.

outflowing gas means that a momentum and energy transfer from the outflow to the wall is possible.

Properties of the high velocity molecular gas can be estimated from the CO(3–2) data. The total velocity range of the CO(3–2) emission is from about  $-30 \text{ km s}^{-1}$  to about  $40 \text{ km s}^{-1}$ . The systemic velocity of the driving source is about  $5 \text{ km s}^{-1}$  (Zinchenko et al. 2015). There are different estimates of the inclination angle in this system but most probably it is rather large, about  $80^\circ$  (Boley et al. 2013; Cesaroni et al. 2018). In this case the maximum outflow velocity is about  $200 \text{ km s}^{-1}$ . At the same time the characteristic outflow velocity as defined

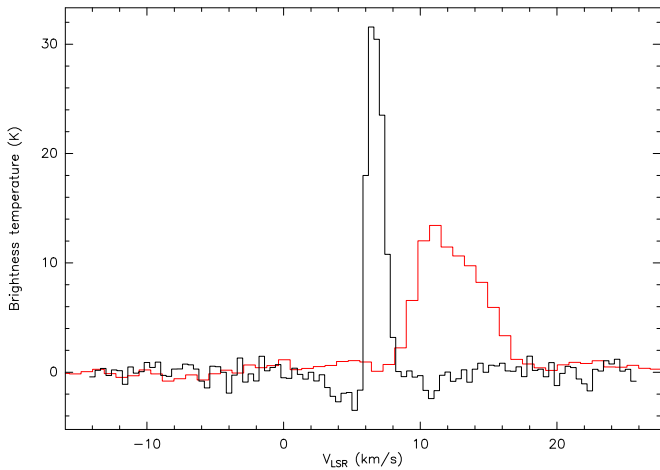


**Figure 10.** SiO(8–7) (red line) and C<sup>34</sup>S(7–6) (black line) spectra averaged over the yellow circle in Figure 9.

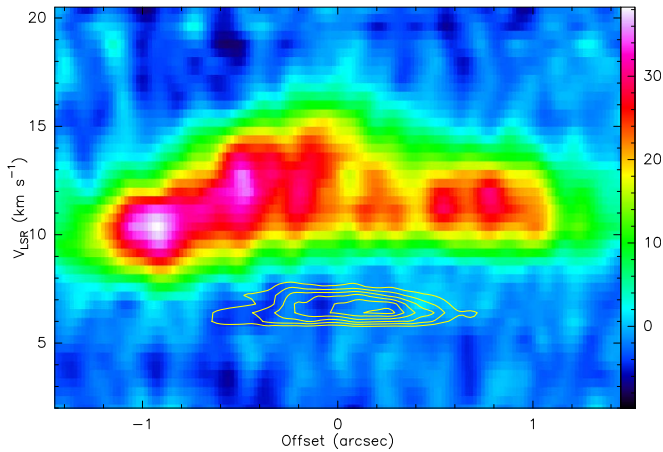


**Figure 11.** Position–velocity diagrams for the SiO(8–7) (image) and C<sup>34</sup>S(7–6) (contours) along the line shown in Figure 9. The negative offsets correspond to the SE direction. The color wedge shows the SiO intensity in mJy beam<sup>-1</sup>. The contour levels are from 0.2 to 0.95 in step of 0.15 of the peak C<sup>34</sup>S intensity, which is 58 mJy beam<sup>-1</sup>.

by Bally & Lada (1983; see also Cabrit & Bertout 1990) is  $\sim 58 \text{ km s}^{-1}$  for the redshifted lobe and  $\sim 50 \text{ km s}^{-1}$  for the blueshifted lobe. Taking the spatial extent of the redshifted outflow lobe about 8000 au (as marked by the Fe II/radio knot) we obtain the outflow dynamic timescale of about 700 yr. It is worth mentioning that for the SW radio knot Cesaroni et al. (2018) found the velocity of  $\sim 660 \text{ km s}^{-1}$  from the variations of its morphology on the time interval of 26 yr. However, they found no variations for the NE knot and noticed that the ejections can be asymmetric. For the further estimates we use the obtained estimate of the dynamic timescale of 700 yr for the redshifted lobe.

Here we consider local properties of the redshifted outflow lobe in the interaction zone near the position marked by the yellow circle in Figure 8. The brightness temperature in CO is  $\sim 100 \text{ K}$ . From the red wing of the CO(3–2) spectrum we obtain the CO column density  $N(\text{CO}) \gtrsim 1.3 \times 10^{18} \text{ cm}^{-2}$  under the assumptions of the LTE conditions and low optical depth, which translates into  $N(\text{H}_2) \gtrsim 1.3 \times 10^{22} \text{ cm}^{-2}$ . The thickness of the emission layer seems to be no larger than 2000–3000 au. Then, the volume density of the high velocity

gas is  $\gtrsim 3 \times 10^5 \text{ cm}^{-3}$ . Such high density is consistent with our previous observations of the HCN (4–3), HCO<sup>+</sup>(4–3) and CS(7–6) emission in this outflow (Zinchenko et al. 2015). This estimate shows that the density contrast between the walls and the high velocity gas is not high, probably less than an order of magnitude.

The total mass of the high velocity gas estimated from the flux in the CO line wings integrated over the outflow region is  $\gtrsim 0.3 M_{\odot}$  (assuming a low optical depth). The upper limit for this estimate is determined by the CO excitation temperature. For example, for  $T_{\text{ex}}(\text{CO}) = 300 \text{ K}$  the outflow mass estimate is  $\sim 0.6 M_{\odot}$  (still assuming a low optical depth). For the outflow dynamic timescale of 700 yr this estimate gives the mass loss rate  $\dot{M} \gtrsim 4 \times 10^{-4} M_{\odot} \text{ yr}^{-1}$ . Wang et al. (2011) estimated the total mass of the outflow from the single-dish observations at  $2.9 M_{\odot}$ . However, this estimate refers to much larger scales, which greatly exceed the field of view of the current observations and does not separate the outflows from the SMA1 and SMA2. The mass loss rate obtained by Wang et al. (2011) is the same as the lower limit given above.

From the comparison of the SiO(8–7) and CO(3–2) intensities at the same velocities, under the assumption of the LTE conditions and low optical depth for both molecules, we obtain the SiO abundance relative to CO  $N(\text{SiO})/N(\text{CO}) \sim 10^{-4}$ . This implies the SiO abundance relative to hydrogen  $X(\text{SiO}) \sim 10^{-8}$ , which represents an enhancement in comparison with a quiescent gas by at least 3 orders of magnitude (Martin-Pintado et al. 1992). This value is close to the highest SiO abundances observed in the outflows in HMSF regions (e.g., Tercero et al. 2011; Sánchez-Monge et al. 2013; Hervías-Caimapo et al. 2019). However, the assumption of the LTE conditions is probably not valid for SiO. The deviations from LTE will make the estimate of the SiO abundance even higher. Our modeling with RADEX (van der Tak et al. 2007) shows that under these conditions the optical depth for both SiO and CO transitions is moderate ( $\lesssim 1$ ) and should not significantly influence the results.

The projected velocity difference between the wall and the high velocity gas reaches  $v \approx 10 \text{ km s}^{-1}$ . Although the high velocity gas should move mainly along the wall, the extent of the SiO emission perpendicular to the outflow direction implies a significant transverse velocity. This is expected for an adiabatic bow shock (Masson & Chernin 1993), which we probably observe in SiO.

The thickness of the walls seen in C<sup>34</sup>S and CCH is about the same as the width of the continuum filamentary structure, i.e.,  $\sim 1000\text{--}2000 \text{ au}$ . The gas velocity dispersion in the walls is low. The C<sup>34</sup>S line width for the spectrum shown in Figure 10 is approximately  $1.2 \text{ km s}^{-1}$ , which corresponds to the one-dimensional velocity dispersion of about  $0.5 \text{ km s}^{-1}$ . This velocity dispersion is mostly nonthermal, since the thermal dispersion for C<sup>34</sup>S is about  $0.13 \text{ km s}^{-1}$  at 100 K. However, it is lower than or comparable to the sound speed, which is approximately  $0.6 \text{ km s}^{-1}$  at 100 K (for the mean molecular weight per free particle  $\mu = 2.33$ ).

An important question is whether these walls are created by the observed outflowing gas or have been created earlier and channel the outflow. The general morphology of these structures in comparison with the distribution of the high velocity gas suggests that the walls immediately surrounding the observed outflow are probably created by this outflow or at least strongly influenced by it. At the same time Figure 8 makes

an impression that in some parts the high velocity gas encounters preexisting dense clumps traced in the  $C^{34}S$  line. The central source demonstrates signatures of episodic bursts. In Figures 4 and 5 we can see arc-like structures which are not related to the currently observed outflow. They may well be remnants of the previous events. It is not excluded that in the past there could have been wind streams from the SMA1 directed to the north (as we see now in the south). Such streams could trigger star formation at the SMA2 site. Of course, this is just a speculation.

The next obvious question is how long such walls can survive. They are probably not gravitationally bound and will disperse in about a crossing time  $t_c \sim L/\sigma_v$ , where  $L$  is the thickness and  $\sigma_v$  is the velocity dispersion. Taking  $L \sim 1000$  au and  $\sigma_v \sim 0.5$  km s $^{-1}$ , as follows from the  $C^{34}S$  data, we obtain  $t_c \sim 10^4$  yr. The age of the currently observed outflow, estimated from its extension and velocity, is apparently much lower, not more than  $\sim 10^3$  yr. The low velocity dispersion in the walls may be explained by the rapid decay of the supersonic turbulence.

A related question is how long we can see the  $C^{34}S$  and CCH emission after the influence of the outflow disappears. The answer depends on the cool-down time and the chemical evolution. In the case of dust cooling the cool-down time in the optically thin regime can be very short (Banerjee et al. 2006). However, it requires a tight thermal coupling between gas and dust for efficient gas cooling, which is achieved at  $n \gtrsim 10^{7-8}$  cm $^{-3}$ . Since the density in the walls seems to be lower, gas can keep a higher temperature than the dust. Then, we estimated the optical depth of the continuum “filament” at  $\sim 0.05$ . For the  $\lambda^{-2}$  dependence of the optical depth, this structure will be opaque at the peak of the dust emission ( $\sim 50$   $\mu$ m for  $T_d \sim 50$  K). The dust column density in the walls is apparently lower but even if it is lower by an order of magnitude, they will be opaque, too. Therefore, the dust cooling may be not very effective here. The cooling rates for molecular cooling calculated by Neufeld et al. (1995) imply the cool-down time for our conditions of several thousand years, i.e., comparable to the dispersion time. A typical chemical evolution time is of the same order of magnitude (e.g Burkhardt et al. 2019). Therefore, episodic ejections with intervals of  $\lesssim 1000$  yr could create the observed structure.

#### 4.3. SMA2

Our ALMA data show a well-collimated high velocity extended outflow from SMA2, which is almost parallel (in projection) to the outflow from SMA1. It is not clear what is happening on the larger scales. The previous SMA and IRAM-30 m data (Wang et al. 2011; Zinchenko et al. 2015) show a single outflow from the S255IR complex at larger distances. It is not excluded that the outflows from SMA1 and SMA2 can merge.

The close-up view of the SMA2 region is shown in Figure 12. Here the map of the first moment of the  $C^{34}S(7-6)$  emission is overlaid with the contours of the CO(3-2) outflow and 0.9 mm continuum emission. In  $C^{34}S$  we see a compact core with an apparent velocity gradient. Both the continuum and  $C^{34}S(7-6)$  integrated intensity maps show an elongated structure with the position angle of the major axis about  $150^\circ$ – $160^\circ$ . However, the position angle of the velocity gradient seems to be different. The size in continuum is  $\sim 0''.37 \times 0''.25$  ( $\sim 670 \times 450$  au). The flux density in continuum is about 60 mJy. The kinematics of

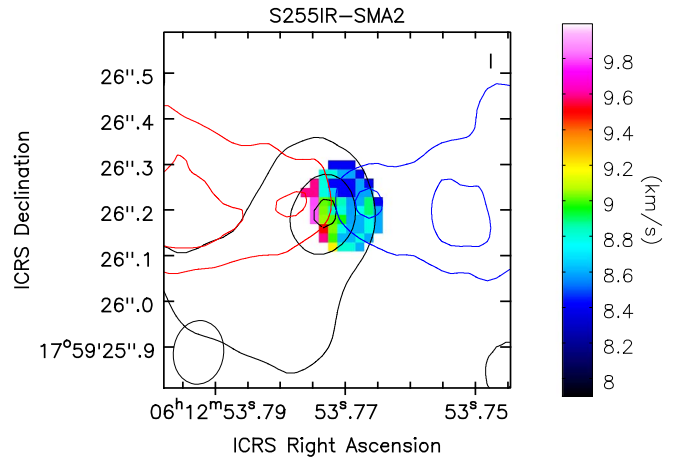


**Figure 12.** Map of the  $C^{34}S(7-6)$  first moment toward the SMA2 core overlaid with contours of the CO(3-2) high velocity redshifted and blueshifted emission (red and blue contours, respectively) and 0.9 mm continuum emission (black). The contour levels are at 8, 12, and 16 mJy beam $^{-1}$  for continuum, at 0.3 and 0.6 Jy beam $^{-1}$  km s $^{-1}$  for the redshifted CO emission and at 0.17 and 0.34 Jy beam $^{-1}$  km s $^{-1}$  for the blueshifted CO emission. The ALMA beam for  $C^{34}S(7-6)$  is shown in the lower left corner.

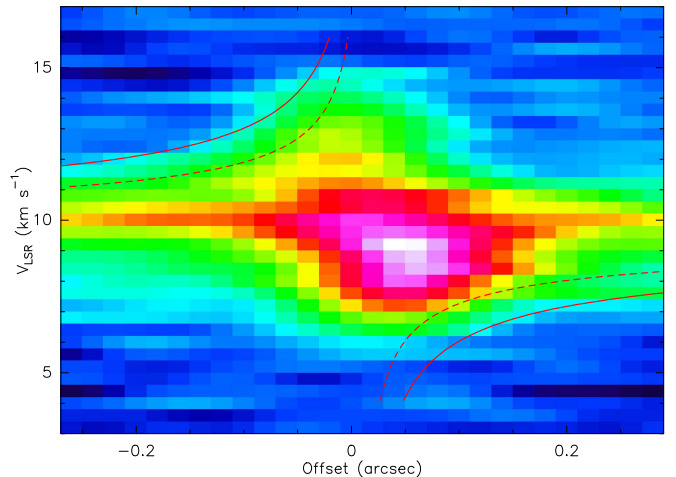


**Figure 13.** Position-velocity diagram in the  $C^{34}S(7-6)$  line along the major axis of the SMA2 core ( $PA = 150^\circ$ ). The curves correspond to Keplerian rotation around the central mass of  $M \sin^2 i = 2.2 M_\odot$  (solid) and  $M \sin^2 i = 1.5 M_\odot$  (dashed).

this core is illustrated in more detail in Figure 13, where we present the position-velocity diagram for this core along the major axis in the  $C^{34}S(7-6)$  line.

The data are consistent with the assumption of a Keplerian-like rotation of the core. Apparently it resembles a disk, although the achieved spatial resolution is not sufficient for a firm conclusion. The continuum flux gives an estimate of the disk mass  $\sim 0.4 M_\odot$  (assuming the dust temperature of 50 K and a normal gas-to-dust mass ratio of 100). For the measured size of SMA2 this mass implies the mean gas density of  $n \sim 3 \times 10^8$  cm $^{-3}$ . At the same time the dynamical central mass obtained from the rotation velocity is much higher,  $M \sin^2 i \sim 2 M_\odot$ , where  $i$  is the inclination angle (Figure 13).

The observed aspect ratio for this core indicates a substantial inclination of the probable disk. However, it hardly can be as large as assumed for the SMA1 core ( $\sim 80^\circ$ ) because in this case the terminal velocity of the molecular outflow would reach

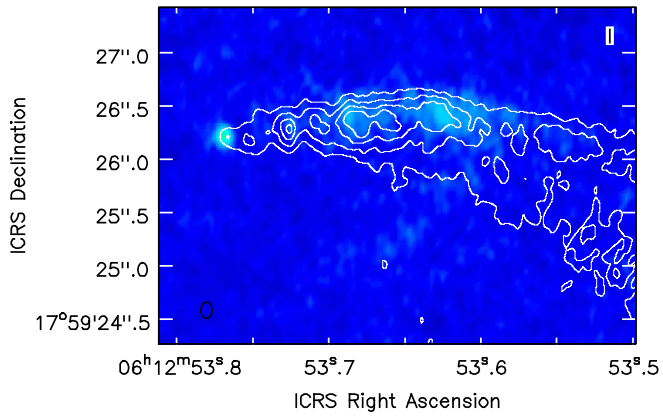


**Figure 14.** Image of the blueshifted outflow lobe from SMA2 in the SiO(8–7) line emission. The velocity range is from  $-42$  to  $-9$   $\text{km s}^{-1}$ . The contours show the high velocity blueshifted CO emission. The contour levels are from 0.2 to 1.0 in step of 0.2  $\text{Jy beam}^{-1} \text{ km s}^{-1}$ .

$\sim 400$   $\text{km s}^{-1}$  and the characteristic velocity  $\sim 300$   $\text{km s}^{-1}$ , which looks unrealistic. For the inclination angle of  $\sim 70^\circ$  these values will be approximately 2 times lower and close to the highest reported values for the outflows (e.g., Bachiller & Cernicharo 1990). From Figure 7 it is evident that the peak outflow velocity increases with the distance from the driving source, which is rather usual for molecular outflows (Arce et al. 2007).

We see a rather strong SiO(8–7) emission in the blueshifted outflow lobe, which correlates well with the CO emission (Figure 14). The enhancement of the SiO abundance here, as indicated by the SiO(8–7)/CO(3–2) intensity ratio, is even higher (by a factor of  $\sim 3$ ) than in the shocked region in the outflow from SMA1. However, no noticeable SiO emission is observed from the redshifted lobe. Distribution of the  $\text{C}^{34}\text{S}(7-6)$  emission (Figure 4) hints that the blueshifted lobe probably propagates in a denser medium, containing more dust. This can explain a higher SiO abundance in this lobe due to the dust grain destruction.

The high collimation of the outflow and the Hubble-type velocity-distance relation imply a jet-driven bow shock model for the outflow (Arce et al. 2007). The outflow is apparently bent (Figures 4, 14). Such bending can be interpreted as a result of disk precession induced by misalignment between the disk and the orbital plane in a binary system taking into account that jets are always launched perpendicular to the disk plane (Monin et al. 2007).

Then, it is easy to see that the outflow from SMA2 consists of a chain of knots separated by about  $0''.2-0''.3$ , i.e., 350–500 au. This most likely indicates periodic ejections from the central object. The velocities of the knots closest to the driving source are apparently significantly lower than the terminal and characteristic velocities mentioned above (Figure 7). They imply the velocities in the plane of the sky  $\sim 30$   $\text{km s}^{-1}$ , which gives the time interval between these ejections  $\sim 50-80$  yr. This can be related to some periodic process in this system, perhaps to the orbital period.

In general, in SMA2 we may witness the formation of a binary system consisting of low- or intermediate-mass stars.

#### 4.4. SMA3

The SMA3 core is associated with the NIRS1 infrared source (Tamura et al. 1991). The measured flux in continuum at 0.9 mm

implies the mass of this core  $\sim 0.3 M_\odot$  (under the previous assumptions about the dust properties and assuming the dust temperature of 50 K). The deconvolved size of the continuum source is approximately  $0''.1$  (Table 1), i.e., about 180 au and no elongation is seen. The corresponding mean gas density is very high,  $n \sim 10^{10} \text{ cm}^{-3}$ . However, the dust temperature in vicinity of this luminous IR source can be higher than assumed above. Then the estimates of the mass and density will be correspondingly lower. No clear velocity gradient is observed in the  $\text{C}^{34}\text{S}(7-6)$  line. In general the source looks isolated and not related to the filamentary continuum structure discussed above.

The NIR polarization measurements show convincing evidence for a bent “S-shape” outflow from this object oriented approximately in the south–north direction (Simpson et al. 2009). On this basis Simpson et al. (2009) suggested that this can be a part of a binary. However, our data do not indicate any molecular outflow from this core. A reasonable assumption is that the outflow lies in the plane of the sky, so that we do not see any high velocity emission and at velocities close to the systemic one the morphology of the CO emission is too complicated.

#### 4.5. New Cores

The newly detected cores labeled here as SMM1 and SMM2 (Figure 1, Table 1) have flux densities at 0.9 mm of 15 and 10 mJy, respectively. These values correspond to masses of  $\sim 0.3 M_\odot$  and  $\sim 0.2 M_\odot$ , respectively (assuming the dust temperature of 20 K). The mean gas density for these cores is  $n \sim 3 \times 10^9 \text{ cm}^{-3}$ . We see no molecular emission clearly associated with these cores. This means that the molecules may be frozen on the dust grains. The absence of the line emission does not allow an estimation of the virial mass but the appearance of the cores suggests that they are probably gravitationally bound. At the same time they have no embedded IR sources. They may represent low-mass prestellar cores according to the widely adopted classification (Andre et al. 2000; di Francesco et al. 2007).

## 5. Conclusions

The main results of this study are the following.

1. Our data show a wide-angle molecular outflow from the massive YSO S255 NIRS3, embedded in the dense core S255IR-SMA1. The outflow dynamic timescale is  $\sim 700$  yr. This wide-angle outflow surrounds the narrow jet traced at the IR wavelengths and in radio continuum. There are bow shocks at the ends of the jet observed in the radio continuum and in the Fe II emission. The CO emission is weak along the outflow axis and peaks near the outflow walls. There are other shocks at the ends of the CO high velocity flows, observed in the SiO (8–7) line. The SiO abundance there is enhanced by at least 3 orders of magnitude. The density of the high velocity gas is  $\gtrsim 4 \times 10^5 \text{ cm}^{-3}$ .

2. We detected warm and dense walls around this wide-angle molecular outflow. The walls are observed in the  $\text{C}^{34}\text{S}(7-6)$  and  $\text{CCH } N = 4 - 3$  lines. The gas temperature in the walls is at least  $\sim 50$  K as indicated by the line brightness temperature, perhaps  $\gtrsim 100$  K, as follows from the apparently high CS abundance. The thickness of the walls is  $\sim 1000-2000$  au. The walls are nonuniform. There are signs of the interaction between the high velocity outflowing gas and the walls.

In addition to the walls surrounding the observed outflow, there are similar structures not associated with the currently

observed outflow. They may represent remnants of the previous ejection events.

3. In continuum at 0.9 mm we see a very narrow ( $\sim 1000\text{--}1800$  au) and dense ( $n \sim 3 \times 10^7 \text{ cm}^{-3}$  assuming the cylindrical geometry) filamentary structure with at least two velocity components. The mass estimated from the continuum emission is about  $35 M_{\odot}$ . The SMA1 and SMA2 cores are apparently associated with this structure, while the SMA3 core looks isolated. The nature of this continuum structure is not quite clear. It may be influenced by both redshifted and blueshifted outflow lobes and it is not excluded that it is a part of the outflow walls.

4. The CO(3–2) data show a collimated and extended high velocity outflow from another dense core in this area, SMA2. The outflow direction in projection is approximately parallel to the outflow from SMA1. The SMA2 core is elongated and rotating in accordance with the Keplerian law. The central mass is  $M \gtrsim 2 M_{\odot}$ , while the mass of the probable disk is  $\sim 0.4 M_{\odot}$ . We see a rather strong SiO(8–7) emission in the blueshifted outflow lobe. The outflow from SMA2 consists of a chain of knots separated by about  $0''.2\text{--}0''.3$ , i.e., 350–500 au. This most likely indicates periodic ejections from the central object with the period of 30–50 yr.

5. The SMA3 core is associated with the NIRS1 infrared source. The measured flux in continuum at 0.9 mm implies the mass of this core  $\sim 0.3 M_{\odot}$  (assuming the dust temperature of 50 K). Although the NIR polarization measurements show convincing evidence for an outflow from this object, our data do not indicate any molecular outflow from this core. A reasonable assumption is that the outflow lies in the plane of the sky.

6. We detected two new compact cores in this area with masses  $\sim 0.2\text{--}0.3 M_{\odot}$  and sizes  $\sim 200\text{--}300$  au. Their mean gas densities are  $n \sim 3 \times 10^9 \text{ cm}^{-3}$ . They may represent low-mass prestellar cores.

We are grateful to the anonymous referee for the detailed and constructive comments, which helped to improve the paper. This research was supported by the Russian Science Foundation (grant No. 17-12-01256) in the part of the data analysis and by the Russian Foundation for Basic Research (grant 18-02-00660) at the data reduction. S.-Y.L. and Y.-N.S. acknowledge the support by the Minister of Science and Technology of Taiwan (MOST 108-2112-M-001-048). This paper makes use of the following ALMA data: ADS/JAO.ALMA#2015.1.00500.S. ALMA is a partnership of ESO (representing its member states), NSF (USA) and NINS (Japan), together with NRC (Canada), MOST and ASIAA (Taiwan), and KASI (Republic of Korea), in cooperation with the Republic of Chile. The Joint ALMA Observatory is operated by ESO, AUI/NRAO and NAOJ.

### ORCID iDs

Igor I. Zinchenko  <https://orcid.org/0000-0003-2793-8229>  
 Sheng-Yuan Liu  <https://orcid.org/0000-0003-4603-7119>  
 Kuo-Song Wang  <https://orcid.org/0000-0002-9323-0950>  
 Yuan Wang  <https://orcid.org/0000-0003-2226-4384>

### References

André, P., Di Francesco, J., Ward-Thompson, D., et al. 2014, *Protostars and Planets VI*, 27  
 André, P., Ward-Thompson, D., & Barsony, M. 2000, arXiv:astro-ph/9903284

Anglada, G., Rodríguez, L. F., & Carrasco-González, C. 2018, *A&ARv*, 26, 3  
 Arce, H. G., Shepherd, D., Gueth, F., et al. 2007, in *Protostars and Planets V*, ed. B. Reipurth, D. Jewitt, & K. Keil (Tucson, AZ: Univ. Arizona Press), 245  
 Bachiller, R., & Cernicharo, J. 1990, *A&A*, 239, 276  
 Bally, J., & Lada, C. J. 1983, *ApJ*, 265, 824  
 Banerjee, R., Pudritz, R. E., & Anderson, D. W. 2006, *MNRAS*, 373, 1091  
 Boley, P. A., Linz, H., van Boekel, R., et al. 2013, *A&A*, 558, A24  
 Bruderer, S., Benz, A. O., Bourke, T. L., & Doty, S. D. 2009a, *A&A*, 503, L13  
 Bruderer, S., Benz, A. O., Doty, S. D., van Dishoeck, E. F., & Bourke, T. L. 2009b, *ApJ*, 700, 872  
 Burkhardt, A. M., Shingledecker, C. N., Le Gal, R., et al. 2019, *ApJ*, 881, 32  
 Burns, R. A., Handa, T., Nagayama, T., Sunada, K., & Omodaka, T. 2016, *MNRAS*, 460, 283  
 Cabrit, S., & Bertout, C. 1990, *ApJ*, 348, 530  
 Caratti O Garatti, A., Stecklum, B., Garcia Lopez, R., et al. 2017, *NatPh*, 13, 276  
 Cesaroni, R., Moscadelli, L., Neri, R., et al. 2018, *A&A*, 612, A103  
 Codella, C., Cabrit, S., Gueth, F., et al. 2014, *A&A*, 568, L5  
 di Francesco, J., Evans, N. J. I., Caselli, P., et al. 2007, in *Protostars and Planets V*, ed. B. Reipurth, D. Jewitt, & K. Keil (Tucson, AZ: Univ. Arizona Press), 17  
 Endres, C. P., Schlemmer, S., Schilke, P., Stutzki, J., & Müller, H. S. P. 2016, *JMoSp*, 327, 95  
 Gómez-Ruiz, A. I., Codella, C., Lefloch, B., et al. 2015, *MNRAS*, 446, 3346  
 Hatchell, J., Fuller, G. A., & Ladd, E. F. 1999, *A&A*, 344, 687  
 Hervías-Caimapo, C., Merello, M., Bronfman, L., et al. 2019, *ApJ*, 872, 200  
 Howard, E. M., Pipher, J. L., & Forrest, W. J. 1997, *ApJ*, 481, 327  
 Hunter, T. R., Brogan, C. L., MacLeod, G., et al. 2017, *ApJL*, 837, L29  
 Kauffmann, J., Bertoldi, F., Bourke, T. L., Evans, N. J., II, & Lee, C. W. 2008, *A&A*, 487, 993  
 Krumholz, M. R. 2012, in *ASP Conf. Ser. 464, Circumstellar Dynamics at High Resolution*, ed. A. C. Carciofi & T. Rivinius (San Francisco, CA: ASP), 339  
 Krumholz, M. R., Klein, R. I., McKee, C. F., Offner, S. S. R., & Cunningham, A. J. 2009, *Sci*, 323, 754  
 Leung, G. Y. C., Lim, J., & Takakuwa, S. 2016, *ApJ*, 833, 55  
 Li, G.-X., Urquhart, J. S., Leurini, S., et al. 2016, *A&A*, 591, A5  
 Liu, S.-Y., Su, Y.-N., Zinchenko, I., Wang, K.-S., & Wang, Y. 2018, *ApJL*, 863, L12  
 Sánchez-Monge, Á., López-Sepulcre, A., Cesaroni, R., et al. 2013, *A&A*, 557, A94  
 Mangum, J. G., & Shirley, Y. L. 2015, *PASP*, 127, 266  
 Martín-Pintado, J., Bachiller, R., & Fuente, A. 1992, *A&A*, 254, 315  
 Masson, C. R., & Chernin, L. M. 1993, *ApJ*, 414, 230  
 McKee, C. F., & Ostriker, E. C. 2007, *ARA&A*, 45, 565  
 Meyer, D. M. A., Vorobyov, E. I., Elbakyan, V. G., et al. 2019, *MNRAS*, 482, 5459  
 Meyer, D. M.-A., Vorobyov, E. I., Kuiper, R., & Kley, W. 2017, *MNRAS*, 464, L90  
 Monin, J.-L., Clarke, C. J., Prato, L., & McCabe, C. 2007, in *Protostars and Planets V*, ed. B. Reipurth, D. Jewitt, & K. Keil (Tucson, AZ: Univ. Arizona Press), 395  
 Moscadelli, L., Sanna, A., Goddi, C., et al. 2017, *A&A*, 600, L8  
 Motte, F., Bontemps, S., & Louvet, F. 2018, *ARA&A*, 56, 41  
 Müller, H. S. P., Schlöder, F., Stutzki, J., & Winnewisser, G. 2005, *JMoSt*, 742, 215  
 Neufeld, D. A., Lepp, S., & Melnick, G. J. 1995, *ApJS*, 100, 132  
 Ossenkopf, V., & Henning, T. 1994, *A&A*, 291, 943  
 Oya, Y., Sakai, N., Lefloch, B., et al. 2015, *ApJ*, 812, 59  
 Oya, Y., Sakai, N., Watanabe, Y., et al. 2018, *ApJ*, 863, 72  
 Shirley, Y. L. 2015, *PASP*, 127, 299  
 Shirley, Y. L., Evans, N. J., II, Young, K. E., Knez, C., & Jaffe, D. T. 2003, *ApJS*, 149, 375  
 Simpson, J. P., Burton, M. G., Colgan, S. W. J., et al. 2009, *ApJ*, 700, 1488  
 Szymczak, M., Olech, M., Wolak, P., Gérard, E., & Bartkiewicz, A. 2018, *A&A*, 617, A80  
 Tamura, M., Gatley, I., Joyce, R. R., et al. 1991, *ApJ*, 378, 611  
 Tan, J. C., Beltrán, M. T., Caselli, P., et al. 2014, in *Protostars and Planets VI*, ed. H. Beuther et al. (Tucson, AZ: Univ. Arizona Press), 149  
 Tercero, B., Vincent, L., Cernicharo, J., Viti, S., & Marcelino, N. 2011, *A&A*, 528, A26  
 Torrelles, J. M., Patel, N. A., Curiel, S., et al. 2011, *MNRAS*, 410, 627  
 Uchiyama, M., Yamashita, T., Sugiyama, K., et al. 2019, *PASJ*, 129  
 van der Tak, F. F. S., Black, J. H., Schöier, F. L., Jansen, D. J., & van Dishoeck, E. F. 2007, *A&A*, 468, 627  
 Wang, Y., Beuther, H., Bik, A., et al. 2011, *A&A*, 527, A32

- Zhang, Y., Higuchi, A. E., Sakai, N., et al. 2018, *ApJ*, 864, 76
- Zinchenko, I., Caselli, P., & Pirogov, L. 2009, *MNRAS*, 395, 2234
- Zinchenko, I., Liu, S.-Y., Su, Y.-N., et al. 2012, *ApJ*, 755, 177
- Zinchenko, I., Liu, S.-Y., Su, Y.-N., et al. 2015, *ApJ*, 810, 10
- Zinchenko, I., Liu, S.-Y., Su, Y.-N., & Sobolev, A. M. 2017, *A&A*, 606, L6
- Zinchenko, I., Liu, S.-Y., Su, Y.-N., & Wang, Y. 2018a, *RAA*, 18, 093
- Zinchenko, I., Liu, S.-Y., Su, Y.-N., & Zemlyanukha, P. 2018b, in *IAU Symp.* 332, *Astrochemistry VII: Through the Cosmos from Galaxies to Planets*, ed. M. Cunningham, T. Millar, & Y. Aikawa (Cambridge: Cambridge Univ. Press), 270
- Zinnecker, H., & Yorke, H. W. 2007, *ARA&A*, 45, 481